Connectivity Defects and Collective Assemblies in Model Metallo-Supramolecular Dual-Network Hydrogels

Mostafa Ahmadi, Lucas Löser, Karl Fischer, Kay Saalwächter, and Sebastian Seiffert*

Double network hydrogels are composed of chemical and physical bonds, whose influences on the macroscopic material properties are convoluted. To decouple these, a model dually crosslinked network with independently tunable permanent and reversible crosslinks is introduced. This is realized by interlinking linear and tetra-arm poly(ethylenegycol) (PEG) precursors with complementary reactive terminal groups. The former also carries a terpyridine ligand at each end, which forms reversible metallo-supramolecular bonds upon addition of metal ions. These dual networks display different types and amounts of network defects, as studied by light scattering and proton double-quantum (DQ) NMR. Dynamic light scattering suggests that the network mesh size decreases upon introduction of metal ions, as supported by a decrease of the residual dipolar coupling constant in NMR. Static light scattering indicates larger static inhomogeneities in those networks composed of stronger ions. This is complemented by a fast solid-like component in the DQ buildup in NMR, attributed to the formation of nanoscopic clusters of charged complexes. The DQ buildup curves also suggest that the presence of strong physical bonds increases the fraction of mobile segments, like loops and dangling ends. This combined study unveils the interplay of chemical and physical bonds toward the formation of a hierarchical structure.

1. Introduction

Double network hydrogels are swollen crosslinked polymers with superior mechanical properties specifically under dynamic deformations.[1] Originally, double network hydrogels were introduced in the form of two interpenetrating chemically crosslinked networks.[2] In these materials, high mechanical strength is obtained when the network has a definite structure, namely, when the first network is densely crosslinked and brittle, whereas the second network is loosely crosslinked and flexible. Under extreme deformation, sacrificial breakage of the chemical bonds in the first network and damping by the strands in the second network act synergistically and significantly increase the mechanical strength and reduce crack propagation.[1] However, the irreversible breakage of the chemical bonds limits their practical applicability. To overcome this limitation, novel double network hydrogels are developed based on physically crosslinked first networks, so that the sacrificial bonds can reform after deformation and the product can be reused.[3,4] Still, like the original double network hydrogels, the optimal elasticity and adaptability can be achieved only with specific structural features.[3–6] Despite this notion, most of the research in this field is devoted to the development of new hydrogels by combination of different types of polymers,[4,6–11] but general structure–property relationships for such materials are less developed as they are for single networks of pure chemical or pure physical crosslinks.

Purely chemically crosslinked networks are generally prepared either by free radical copolymerization of monomers and crosslinker or by connecting pre-polymerized building blocks.[12] Either way, the reaction conditions strongly affect the structure of the gels obtained.[13] In turn, the properties of these gels, as-prepared or in swollen states, depend on the structure and the polymer-network homogeneity, and these are the two main tuning controls.[14,15] Accordingly, Sakai and coworkers have developed new hydrogels based on two complementary tetra-PEG building blocks, which offer a regular network mesh size and therefore a homogeneous structure to be formed that provides superior mechanical strength compared to the typical inhomogeneous hydrogels.[16]

In contrast to such permanent chemical networks, purely physically crosslinked networks have a structure that evolves through time.[17–19] In this context, the dynamics of the reversible bonds determines the rate of structural development in response to external stimuli. Therefore, dynamic characteristics control the final properties of physical gels. Craig and coworkers[20] and

M. Ahmadi
Department of Polymer Engineering and Color Technology
Amirkabir University of Technology
Tehran, Iran
M. Ahmadi, K. Fischer, S. Seiffert
Institute of Physical Chemistry
Johannes Gutenberg-Universität Mainz
Duesbergweg 10-14, D-55128 Mainz, Germany
E-mail: sebastian.seiffert@uni-mainz.de
L. Löser, K. Saalwächter
Institut für Physik-NMR
Martin-Luther-Universität Halle-Wittenberg
Betty-Heimann-Str. 7, D-06120 Halle, Germany

The ORCID identification number(s) for the author(s) of this article can be found under https://doi.org/10.1002/macp.201900400.

**ADVANCED
SCIENCE NEWS**

www.advancedsciencenews.com

**Macromolecular
Chemistry and Physics**

www.mcp-journal.de

later Scherman and coworkers[21,22] have shown that the dissociation rate of the physical bonds, which is connected to the activation energy for breakage of these bonds, controls the rheological behavior of physical polymer networks based on metal–ligand coordination or host–guest interactions, respectively.

When the latter two different kinds of networks are combined in one material, a dual network results, which combines the ability for elastic energy storage of the former with the ability for adaptiveness of the latter. However, in such concert, correlating the characteristics of each network to the final properties is not straightforward. For instance, dynamic light scattering (DLS) studies on classical double network hydrogels showed that while the first network is essentially frozen, the second network shows two relaxation modes: a fast gel mode and a slow translational relaxation mode.[23] The slow diffusion of the second network through the highly crosslinked first network is possible only if big voids are present in the structure of the first. The conclusion of this finding was that the brittle network has a hierarchical structure consisting of highly crosslinked clusters connected by elastically active chains. Sacrificial breakage in the first network happens in a stepwise fashion, starting from the elastically active bonds, proceeding to the highly crosslinked clusters, while the second network can diffuse between these clusters and damp the energy.[23,24] Consequently, inhomogeneity in the structure in the first network was believed to play an important role in the material's performance under dynamic deformation. Surprisingly, similar mechanical properties were obtained after replacing the heterogeneous first network by a homogeneous tetra-PEG hydrogel.[25] This argument highlights the necessity of a precise characterization of the structure and its correlation to the mechanical properties of double network hydrogels. Even more, it is crucial to devise simple model networks, where the contribution of each network component can be independently varied.

To achieve this goal, Sakai and coworkers have developed an amphiphilic dually crosslinked network based on complementary clickable tetra-arm PEG and linear PDMS building blocks.[26–28] Hydrophobic association of the PDMS blocks provides reversible crosslinks. However, the strength of these physical bonds cannot be tuned without compromising the overall structure of the network. To overcome the latter limitation, we have recently combined the tetra-arm PEG chemistry and metal–ligand coordination and developed dual crosslinked model networks with independently tunable network components.[29,30] The mechanical performance of such partly reversible double network hydrogels has been generally proven to compete with that of the original chemically crosslinked ones,[4] and even further enhancement appears possible. For this purpose, however, a rational understanding of the nanostructural constitution, the molecular dynamics, and the macroscopic properties of these hybrid networks is necessary. In this context, our former study of the dynamic properties of these materials showed that the association strength of the metallo-supramolecular bonds is affected by the structure of the chemical network.[30–32] These bonds can also create collective assemblies by formation of nanosized clusters, specifically when strong ions are used.[30] Such associations affect the overall structure of the network. To shed further light on the structure of these materials, here we specifically study the structural inhomogeneities of these

networks with the help of DLS and static light scattering (SLS) and proton double–quantum (DQ) NMR. Our results provide further support for the presence of collective assemblies formed by nanosized clustering of the strong ions.
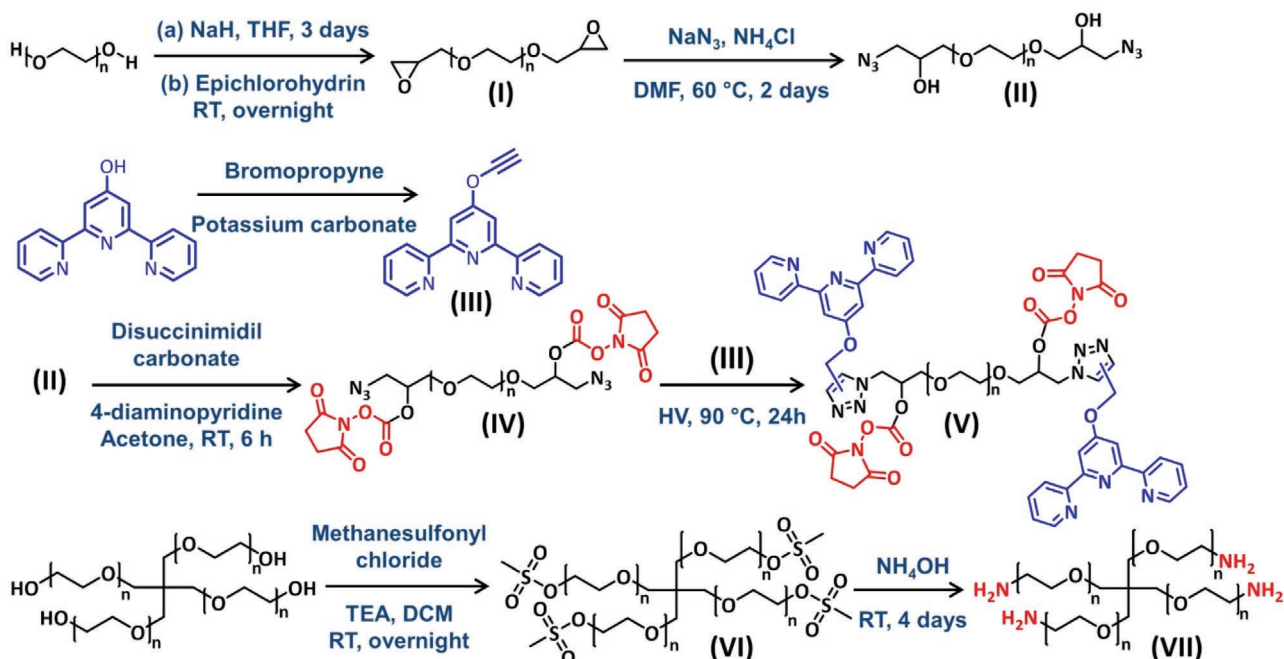
2. Experimental Section

2.1. Materials

Dual-network hydrogels were formed from a 6 kg mol^{-1} linear PEG precursor with terpyridine and *N*-hydroxy succinimide (NHS) ester functionalities at both ends and a 10 kg mol^{-1} amine functionalized tetra-arm PEG precursor. To realize this approach, the linear and the tetra-arm PEG precursors were produced by sequential reaction steps, as shown in **Scheme 1**. Specifically, the linear precursor was first functionalized with an epoxide group, and then the ring was opened by sodium azide, which provided both azide and hydroxyl functionalities. Subsequently, the NHS ester was grafted to the hydroxyl group via a simple substitution reaction, and the propargyl terpyridine was coupled with the azide group through metal-free azide–alkyne Huisgen cycloaddition. The propargyl terpyridine itself was synthesized by reacting commercially available 2,6-bis(2-pyridyl)-4-pyridone and propargyl bromide. For the preparation of the tetra-PEG precursor, the terminal hydroxyl groups were first replaced by mesyl functions and subsequently substituted by amine groups. Details of the reaction conditions and characterization results are described elsewhere.[30]

These two precursors reacted in water and formed covalent bonds by an instantaneous click reaction between the terminal amine and the NHS ester groups, as illustrated in **Figure 1**. The terpyridine ligands formed additional metallo-supramolecular bonds based on metal–ligand coordination upon addition of metal ions. Manganese(II), zinc(II), cobalt(II), and nickel(II) nitrate salts were used, which formed metallo-supramolecular bonds with kinetic stabilities in the order of Mn < Zn < Co < Ni.

2.2. Light Scattering

DLS and SLS were performed utilizing a multi-angular detection setup (ALV CGS 8F SLS/DLS 5022F, ALV-GmbH Langen, Germany) equipped with a He/Ne laser (Uniphase, 25 mW, 632.8 nm) and a single angular detection unit with pseudo-cross correlation layout employing fiber optical beam splitting on two avalanche photodiodes (ALV high QE APD) connected to a ALV7004 hardware correlator (ALV GmbH Langen, Germany). All measurements were performed at (20 ± 0.1) °C with the help of an external thermostat (ThermoFisher CP25) connected to the goniometer cell housing holding a toluene-filled vat for index matching and temperature control of the immersed cylindrical sample cells made from Suprasil quartz glass; these were 10 cm in length and 2 cm in outer diameter, equipped with two stoppers made of Teflon. The lower Teflon stopper (home built) was directly centered above the sample to prevent evaporation, and the upper Teflon cap was custom-made by Hellma, Müllheim Germany. Due to the nonergodicity of the prepared polymer gels, a rotating cuvette holder (custom-made

ADVANCED
SCIENCE NEWS
www.advancedsciencenews.com

Macromolecular
Chemistry and Physics
www.mcp-journal.de

Scheme 1. Synthesis approach for the preparation of a model dual-network hydrogel out of a linear and a tetra-arm PEG precursor: The linear PEG is first functionalized with epoxide rings (I) that are subsequently opened to yield hydroxyl and azide groups at both chain ends (II), which are grafted with NHS ester (IV) and terpyridine ligands (V), respectively. The tetra-arm PEG is functionalized by amine groups through mesylation (VI) and subsequent substitution with ammonia (VII).

CRT-Unit, ALV-GmbH Langen, Germany) was mounted on the goniometer, which enabled us to measure the scattering intensity at several random positions. The angular range was typically covering 30–140° and simultaneous DLS/SLS measurements were performed in 5 to 10° angular step increments with a typical duration time of 30 s for one single run and position, thus allowing for correct baseline measurements with symmetric ergodic normalization (ALV-Correlator software version 3.0). 100 positions were measured at each angle; a protocol written by ALV macro script language controlled the measurement sequence: start rotation (typically 5 s with 0.252 rpm), stop rotation, wait for 5 s (to allow for mechanical relaxation), start

correlation (e.g., 30 s), stop correlation, repeat until number of positions is attained, then change angle by the increment.

Samples were prepared at a concentration of 100 g L^{-1} in a 50 mM PBS phosphate buffer at a pH of 6.75, which controlled the NHS-ester amine reaction to lead to gelation in a range of roughly 10 min; all hydrogel components were separately dissolved in the buffer solution and filtered through Whatman Anotop filters 0.02 μm into dust-free vessels. Equimolar ratios of the precursors and the metal salt solutions were poured into the dust-free cuvettes and mixed by a vortexer. All sample preparation steps were performed in a dust-free laminar flow cabinet (ThermoFisher). The weaker coordinating metal ions
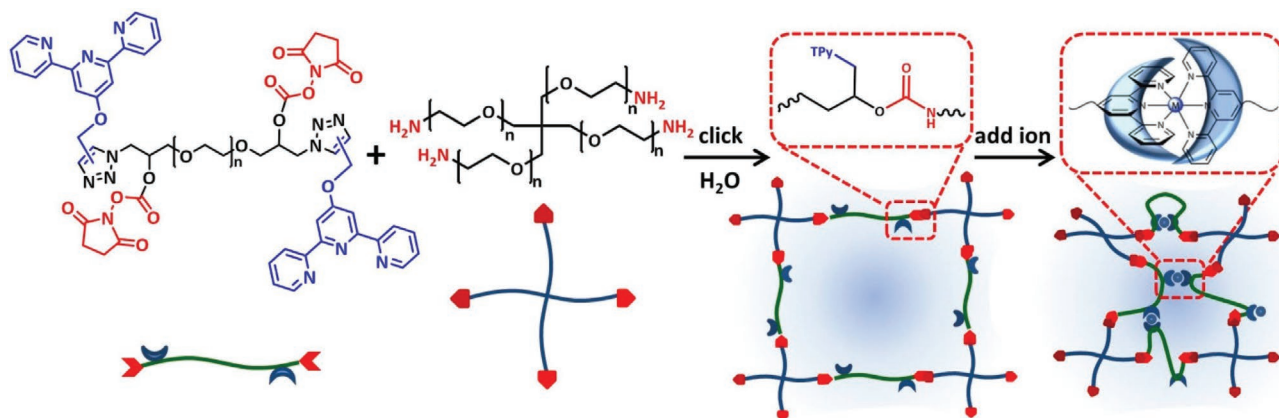

Figure 1. Material basis for the preparation of dually crosslinked networks: a linear PEG precursor carrying a terpyridine and a NHS ester at each end, a tetra-arm PEG precursor containing amine group at each end rapidly form a chemical crosslink in water, and the terpyridine ligands form additional bis-complexes upon addition of metal ions.

**ADVANCED
SCIENCE NEWS**
www.advancedsciencenews.com

**Macromolecular
Chemistry and Physics**
www.mcp-journal.de

easily allowed the escape of air bubbles before solidification, but the strongly coordinating ions, Co^{2+} and Ni^{2+}, immediately increased the viscosity after their addition and thereby prolonged the escape of such bubbles. Therefore, overly strong and long vortexing should be avoided in these cases. To account for this circumstance, samples with weaker coordinating ions were vortexed for 30 s, whereas samples with stronger coordinating ions were vortexed for just 5 s. The cuvettes were then sealed and stored at room temperature for 24 h for complete formation of the chemical and the physical bonds within the hydrogel. All hydrogels obtained by that procedure were highly transparent and weakly scattering, which qualitatively inferred molecular homogeneity of the components.

2.3. ^{1}H DQ NMR

Low-field NMR experiments were performed on a Bruker minister mq20 with a magnetic field of $B_0 = 0.47T$ and 90° and 180° pulse lengths varying between 1.5 and 6 µs. The temperature was held at 40 °C by a BVT3000 unit operating on an air flow. Buildup curves of the longitudinal (T_1) relaxation were measured by a saturation recovery experiment with a variable relaxation delay for quantifying polymer and HDO-signal relaxation times, as well as their relative amounts in the samples (see **Figure 2**). DQ buildup curves and reference decays were measured using the Baum-Pines with incremented delays between the pulses and a constant number of two cycles. The delay between the scans was adjusted to the T_1 of the polymers and HDO signal in such a way that the HDO signal was mostly filtered out. The theoretical leftover amount can be calculated using the saturation-recovery data. Samples with the same concentration as reported for the light scattering measurements were prepared using D_2O phosphate buffer in 1 cm diameter glasses, flame sealed to avoid evaporation.

Longitudinal relaxation times of all samples were measured using the saturation recovery experiment. Fitting the obtained data sets to Equation (1), we obtain a long- and a short-T_1 com-

ponent (and their fractions), which we identify with residual HDO and polymer proton signal, respectively. Knowing the recycle delay (relaxation period during individual scans) for the DQ experiment, which is shorter than the longest T_1 for time-saving reasons, we can straightforwardly calculate the amount of HDO signal that contributes to the measured tail fraction.

$$I_{SatRec}(t) = a_{poly}(1 - \exp(-\tau/T^1_{poly})) + (1 - a_{poly})(1 - \exp(-\tau/T^1_{solv})) \quad (1)$$

Here a short description of the DQ data treatment procedure is given; for further information, the reader is referred to refs. [33,34]. The experimental observables of a DQ-experiment are two phase-cycle-controlled signal functions: the DQ buildup, $I_{DQ}(\tau_{DQ})$, and the reference decay intensity, $I_{ref}(\tau_{DQ})$. The former contains wanted information about the residual dipolar coupling (RDC) constant (D_{res}), which (as described in more detail below) correlates inversely with the network strand length. The latter represents an intensity complement subject to the same relaxation process (T_2 relaxation), which is needed to separate the interplay of structural contributions to the initial DQ buildup curve and signal decay at long times. A point-by-point normalization of I_{DQ} yields a signal that is only dependent on the RDCs and their distribution. It contains additional information on the proton fraction of the non-network mobile polymer segments, as those have usually a significantly longer T_2 (due to their higher mobility) and have no contribution to I_{DQ} (i.e., $D_{res} = 0$). They usually appear as a long-time tail in the I_{ref} and $I_{\Sigma MQ}$ ($I_{ref} + I_{DQ}$) signal are fitted and quantified using a mono- or biexponential function.

$$tail = \sum_{i=1,2} b_i \exp(-\tau_{DQ}/T_{2,i}) \quad (2)$$

After subtraction of the tail from the sum intensity, $I_{\Sigma MQ}$, the normalized relaxation-free DQ buildup curve, $I_{nDQ}(\tau_{DQ})$, can be obtained as

$$I_{nDQ}(\tau_{DQ}) = I_{DQ}(\tau_{DQ})/(I_{\Sigma MQ}(\tau_{DQ}) - tail) \quad (3)$$
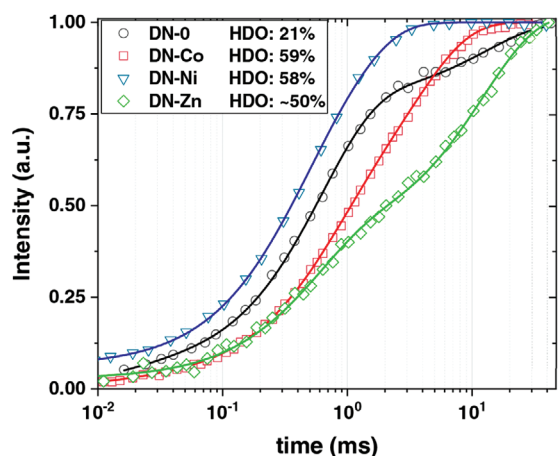
Sample	a_{poly}	T^1_{poly} (s)	a_{solv}	T^1_{solv} (s)
DN-0	76% ± 1%	0.61	24% ± 1%	13 ± 1.5
DN-Zn	60% ± 10%	0.52	40% ± 10%	12 ± 2
DN-Co	40% ± 2%	0.9	60% ± 2%	3.5 ± 0.2
DN-Ni	41% ± 5%	0.2	59% ± 5%	0.9 ± 0.1

Figure 2. a) Buildup of the longitudinal magnetization measured by the saturation recovery experiment for all samples. The solid lines are obtained by fitting of all curves, according to Equation (1). Table: Obtained fit results (fractions for polymer and HDO signal, as well as corresponding T_1 values) for the saturation recovery experiment for all samples. The error of $T_{1,poly}$ was below 1% and is thus not presented.

The normalized DQ build-up curve approaches 0.5 at longer times (per definition), which can be fitted with an "Abragam-like" (A-l) function,[35] to provide the average D_{res}.

$$I_{nDQ}^{A-l}(\tau_{DQ}) = 0.5\{1 - \exp[-(0.378 D_{res}\tau_{DQ})^{1.5}] \times cos(0.583 D_{res}\tau_{DQ})\} \quad (4)$$

When a single function cannot reproduce the shape of the normalized DQ build-up curve, a sum of several A-l functions or even a log-normal distribution of RDC constants can be considered:

$$I_{nDQ}(\tau_{DQ}) = \int_0^\infty I_{nDQ}^{A-l}(\tau_{DQ}) p(\ln D_{res}) d\ln D_{res} \quad (5)$$

The log-normal distribution function $p(\ln D_{res})$ is characterized by the median D_{av} and the logarithmic (i.e., dimensionless) standard deviation σ, which are the free parameters in a numerical integration upon fitting.[36] Another possibility of fitting data that does not depend on the calculation of I_{nDQ} was presented first by Lange,[37] fitting $I_{\Sigma MQ}$ and I_{DQ} simultaneously with a superposition of relaxation functions and relaxing A-l functions, respectively.

$$I_{DQ}(\tau_{DQ}) = \sum_{i=1}^3 a_i I_{nDQ,i}^{A-l} \exp\left[-\left(\frac{\tau_{DQ}}{\tau_i}\right)^{\beta_i}\right] \quad (6)$$

$$I_{\Sigma MQ}(\tau_{DQ}) = \sum_{i=1}^3 a_i \exp\left[-\left(\frac{\tau_{DQ}}{\tau_i}\right)^{\beta_i}\right] \quad (7)$$

As will be discussed later, due to a large spread in RDC values and relaxation times, this approach is required to reliably fit the data obtained from the dual-network hydrogels.

3. Results and Discussion

The studied set of samples includes five dually crosslinked model network hydrogels. The chemical network is formed by complementary A–B type click reaction between the NHS ester and the amine terminal groups of the linear and the tetra-arm PEG precursor, respectively. The extent of crosslinking cannot be quantified by solution ^{1}H NMR due to the peak broadening effect. However, our former rheological studies suggest that the reaction yield should be quantitative.[30] The linear precursor also carries a terpyridine ligand at each end, which forms a bis-complex upon addition of divalent metal ions, as illustrated in Figure 1. The linear precursor also contains triazole rings, which can form metallo-supramolecular bonds;[38,39] however, only one relaxation process is reflected in the dynamic rheological behavior of the corresponding dual networks.[30] This confirms that the weakly coordinating triazole groups cannot compete with the terpyridine ligands to form any discernible metallo-supramolecular bonds. Following our previous approach, we utilize Mn^{2+}, Zn^{2+}, Co^{2+}, and Ni^{2+} nitrate salts to create the metallo-supramolecular linkages.[30] Accordingly, the dual network samples are prepared by mixing an equimolar ratio of the linear and the tetra-arm PEG precursors at an overall polymer concentration of 100 g L^{-1}, and an equimolar amount of metal ions. The samples are coded as DN-X, where X denotes the applied ion, including, Mn, Zn, Co, and Ni, and 0 for the case of a plain chemical network.

The polymer precursor solutions are mixed for about 1 min, immediately followed by addition and mixing of the metal salt solution. We use a vortexer to facilitate mixing on a molecular-level before gelation, which otherwise cannot be achieved by simple diffusion. Traces of dust in cuvettes are avoided by rinsing using an acetone fountain. It is vital for light scattering measurements to avoid any air bubble that may form by mixing and get trapped during the gelation process. Consequently, we increase the gelation time to about 10 min by adjusting the pH value around 6.75 using a phosphate buffer solution.[30] Therefore, the formation of the chemical bonds before addition of metal ions should be negligible. The buffer solution was prepared by mixing appropriate amounts of 0.1 M NaOH and 0.1 M potassium dihydrogen phosphate solutions. Larger pH values give shorter gelation times, while lower pH values result in the hydrolysis of the NHS ester and loss of network connectivity.[30] Even though the ^{1}H DQ NMR technique is not sensitive to dust and air bubbles, a similar procedure is followed for the corresponding sample preparation. Our former study on the dynamics of such dual crosslinked networks shows that strong coordinating ions may form collective assemblies that cause structural inhomogeneities.[30] To assess the presence of such inhomogeneities, we turned to investigating the structure of the selected sample series at different length scales.

The structure of polymer networks inherits inevitable inhomogeneities on local and on global scales.[40] The former consists of network defects like dangling ends, loops, and misconnectivities on length scales of 1–10 nm, while the latter is caused by static spatial concentration fluctuations on scales of 10–100 nm.[14] The local inhomogeneities are the subject of small-angle X-ray and neutron scattering (SAXS and SANS) and ^{1}H DQ NMR studies, while the global inhomogeneities are conventionally studied by light scattering.[14,15,37,41] Accordingly, we use SLS and DLS and ^{1}H DQ NMR, in separate sections, to elucidate the structure of our dually crosslinked networks on the global and local scales, respectively.

3.1. Light Scattering

The scattering of the laser light, passing through a polymer solution or a gel, is caused by local concentration fluctuations. There are two types of concentration fluctuations in a polymer gel. Dynamic concentration fluctuations originate from Brownian motion of the solute in a solution or from the local movement of network strands around their average positions in a gel. These fluctuations are driven by the thermal energy of the system. On top of that, due to the uneven spatial distribution of the crosslinking density, static concentration fluctuations are specifically present in polymer-network gels. That causes a special speckle pattern in the locally resolved time-averaged intensity of the light scattered from a gel. Such data can be analyzed from SLS and DLS perspectives.
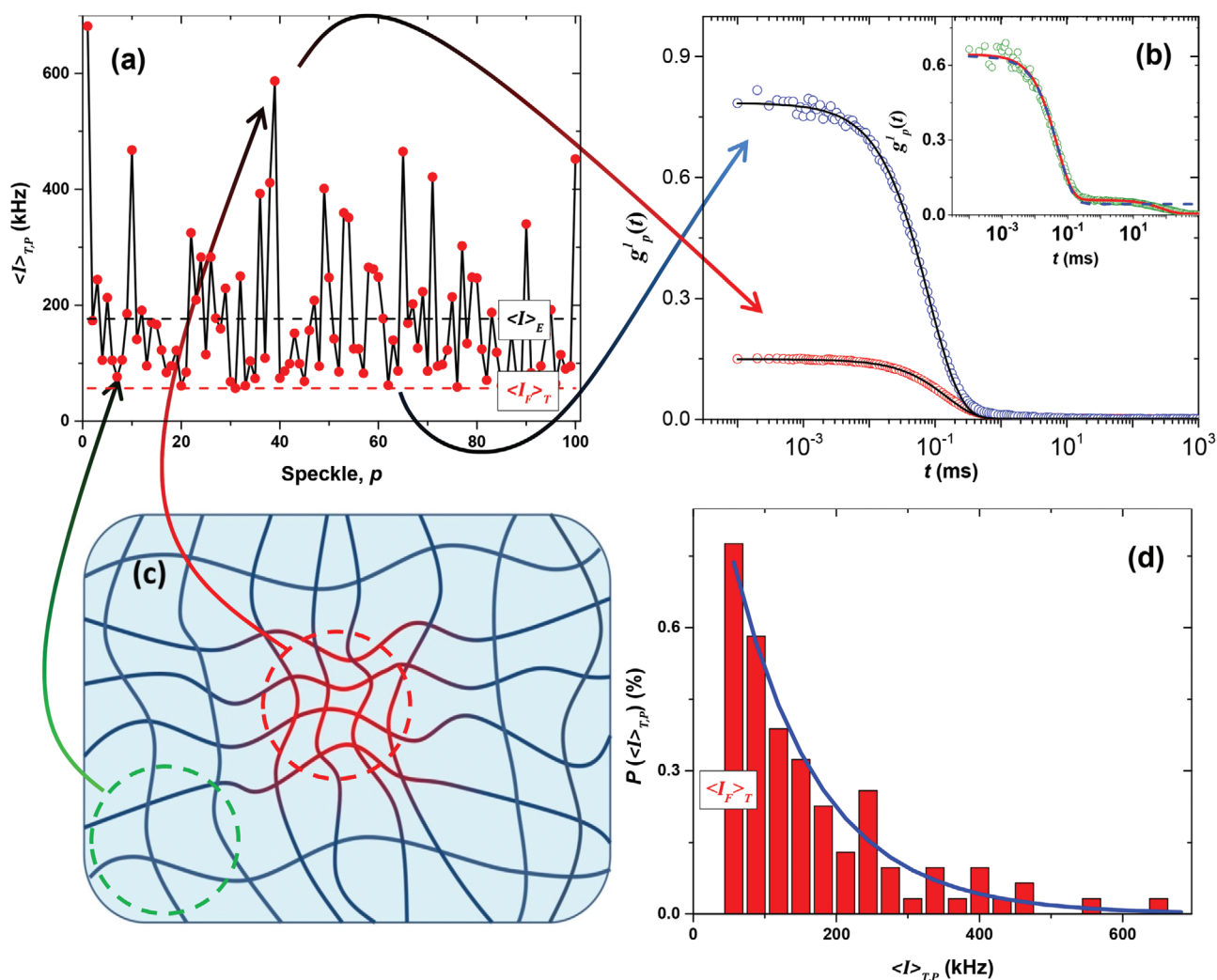
**ADVANCED
SCIENCE NEWS**

www.advancedsciencenews.com

**Macromolecular
Chemistry and Physics**

www.mcp-journal.de

Figure 3. Representative static and dynamic light scattering results of the plain chemical network: a) speckle pattern of the time-average scattering intensity at each position, $\langle I \rangle_{T,P}$ obtained at 60°. The ensemble-average intensity is shown by $\langle I \rangle_E$ and the dynamic scattering contribution is shown by $\langle I_F \rangle_T$. b) Time correlation function of the dynamic scattering component at two speckles of low and high intensity. The solid lines are obtained by a single exponential fitting using Equation (7) according to Joosten's method.[42] The inset plot shows a representative field correlation data of DN-Zn at 60° where a single exponential function (dashed blue line) cannot explain the behavior and a bi-exponential function (solid red line) is required instead. c) The corresponding high and low speckles are illustratively associated with the static concentration fluctuations in the polymer network. d) Histogram of the scattering speckles at 60°. The solid line is provided by Equation (2).

SLS probes the time-averaged scattering intensity as a function of the scattering angle. Wide scattering angles, between 30° and 140°, provide information about concentration fluctuations on scales that give rich insight into the global structural inhomogeneities. We have therefore studied the SLS properties of the dually crosslinked samples. Due to the nonergodicity of the samples, that is, since the locally resolved time-averaged scattering intensities are different from the overall ensemble average, such analysis cannot provide reliable information about the structure, unless a large enough number of points are scanned. In this study, each sample is subjected to scattering from 100 random positions at each angle. The fluctuations in the speckle pattern are shown for the representative case of the plain chemical network (DN-0) at 60° in **Figure 3**a. The time-averaged scattering at each point, $\langle I \rangle_{T,P}$, originates from the thermal and the static fluctuations,

as illustrated in Figure 3c. The minimum of the scattering intensity $\langle I_F \rangle_T$ is expected to be equal to the thermal scattering intensity of the corresponding uncrosslinked solution of the polymer precursors.[15] The histogram of the scattering intensity $P(\langle I \rangle_{T,P})$ can be described by the following single exponential function:

$$P(\langle I \rangle_{T,P}) = \delta(\langle I \rangle_{T,P} - \langle I_F \rangle_T) exp\left(-\frac{\langle I \rangle_{T,P} - \langle I_F \rangle_T}{\langle I \rangle_E - \langle I_F \rangle_T}\right) \quad (8)$$

where δ is the Dirac delta function. The good agreement between the normalized histogram and the calculation made by Equation (8), as shown in Figure 3d, is a qualitative measure of homogeneity.

The outcome of the SLS analysis is the ensemble-average scattering intensity as a function of the scattering vector. The
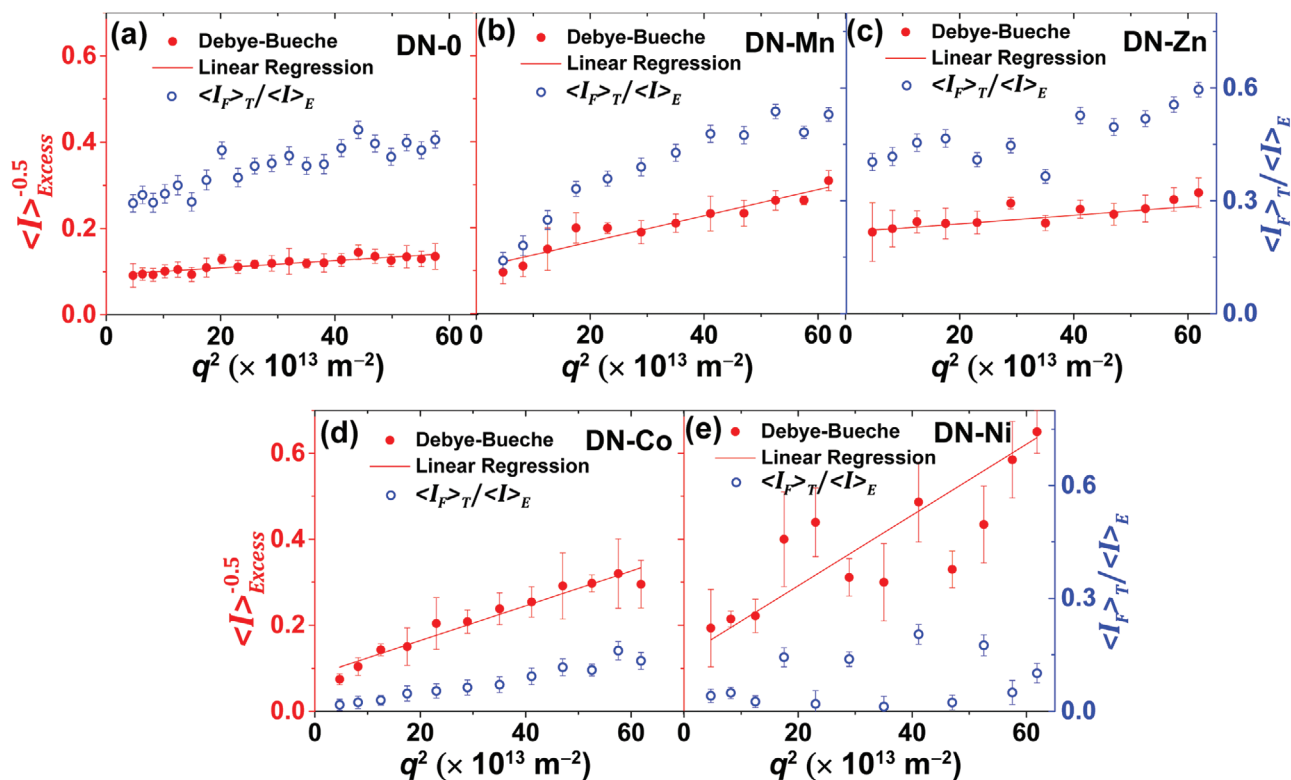
Figure 4. Linearized excess scattering intensity as a function of squared scattering vector according to the Debye–Bueche method[14] for a) DN-0, b) DN-Mn, c) DN-Zn, d) DN-Co, and e) DN-Ni. The right-hand ordinate shows the ratio of the thermal to the overall scattering intensities, as determined from the speckle pattern represented in Figure 3a. Bars represent the standard errors.

difference between the ensemble-average scattering intensity and the thermal scattering intensity at each angle, $I_{excess}(q)$, correlates with the static spatial concentration inhomogeneity according to Debye and Bueche, as described by Equation (9). Linearization of this equation in the form of Equation (10) allows the static correlation length to be determined from the slope, m, and the intercept, b ($\Xi = (m/b)^{0.5}$).[14]

$$I_{excess}(q) = \frac{4\pi K \Xi^3 \langle \eta^2 \rangle}{(1 + q^2 \Xi^2)^2} \tag{9}$$

$$I_{excess}(q)^{-0.5} = (2\sqrt{\pi K \Xi^3 \langle \eta^2 \rangle})^{-1} + 0.5\sqrt{\frac{\Xi}{\pi K \langle \eta^2 \rangle}}\, q^2 \tag{10}$$

The corresponding linearized data are shown for all samples in **Figure 4**. The larger standard error bars for samples made by stronger ions implies that they have more scattered data, probably due to trapped air bubbles that may not be noticeable in the bare sample appearance. Nevertheless, these samples also show larger slopes and correspondingly stronger contributions from the static inhomogeneities. The ratio of the fluidic to the overall scattering intensities against the squared scattering vector, as shown on the right-hand ordinate, has an increasing trend for all samples, which suggests further contribution of thermal fluctuations at smaller length scales. The average $\langle I_F \rangle_T / \langle I \rangle_E$ ratio is lower for DN-Co and DN-Ni samples compared to the others, which reveals that strongly coordinating ions, Co^{2+} and Ni^{2+},

create more static concentration fluctuations than weaker coordinating Zn^{2+} and Mn^{2+} ions.

DLS probes the temporal evolution of concentration fluctuations as calculated by the intensity correlation function, $g_p^2(q,t)$. In ergodic samples, this quantity can be converted to the field correlation function, $g_p^1(q,t)$, using the Siegert relation.[14,15]

$$g_p^1(q,t) = \sqrt{g_p^2(q,t) - 1} \tag{11}$$

In a solution of monodisperse hard spheres, the field correlation function decays in time following a simple exponential function, providing the specific correlation time, τ.

$$g_p^1(q,t) = \exp(-t/\tau) \tag{12}$$

where τ inversely correlates to the diffusion coefficient of the solute.

$$\tau^{-1} = D_{tr}\, q^2 \tag{13}$$

The diffusion coefficient, D_{tr}, in turn, is used to determine the hydrodynamic radius of the solute, according to the Stokes–Einstein equation.

In a polymer gel, however, both dynamic and static concentration fluctuations are present. The field correlation function of the former decays exponentially in time, but the latter is constant. Due to the nonergodicity, their relative contributions
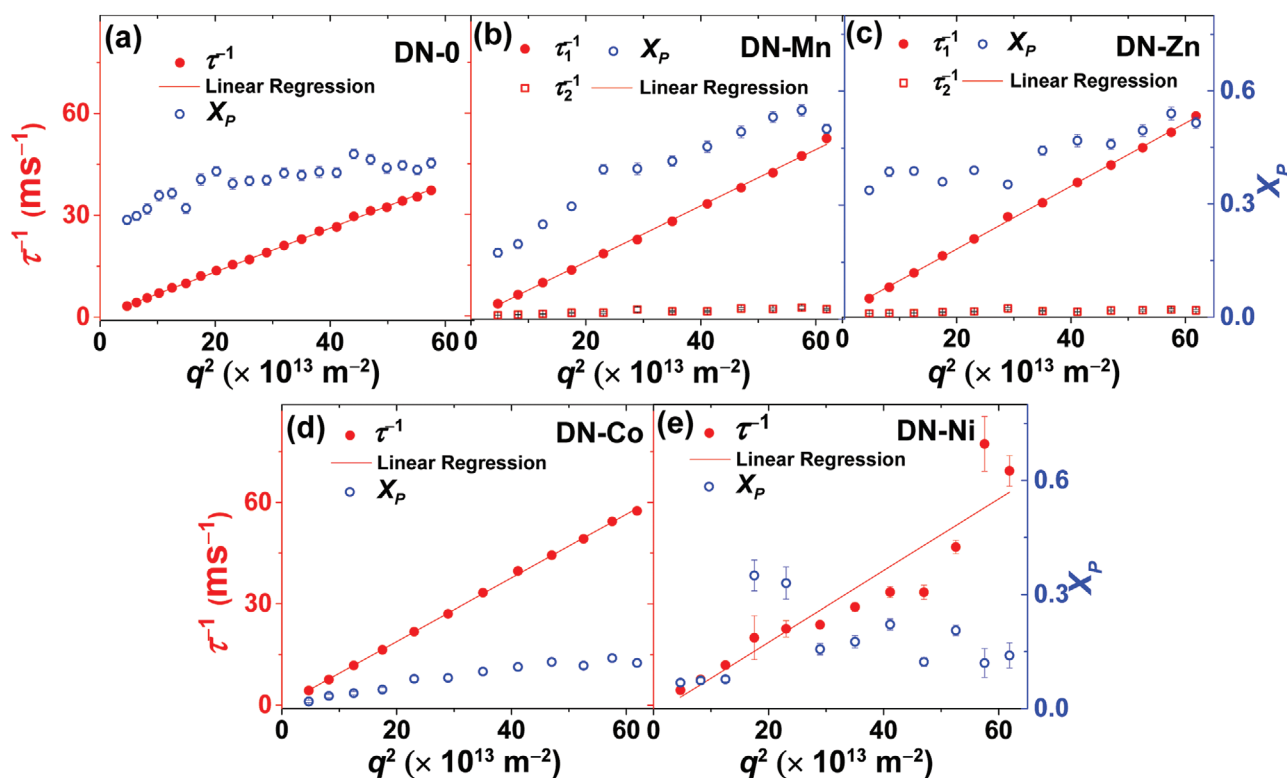
**ADVANCED
SCIENCE NEWS**
www.advancedsciencenews.com

**Macromolecular
Chemistry and Physics**
www.mcp-journal.de

Figure 5. Inverse correlation time against q^2 for a) DN-0, b) DN-Mn, c) DN-Zn, d) DN-Co, and e) DN-Ni. There are two separate relaxation modes for DN-Mn and DN-Zn samples (b and c), denoted by time constants τ_1 and τ_2. The right-hand ordinate shows the ratio of the thermal to the overall scattering intensities. Bars represent the standard errors.

are different at different positions. Accordingly, Equation (11) cannot be used anymore to calculate the field correlation function. Instead, by realizing the inequality of the scattered intensity between the ensemble and the time averages, Joosten and coworkers proposed the partial heterodyne method, which correlates the intensity correlation function to the field correlation function of the dynamic component at every position.[42]

$$g^2_{T,p}(q,t) = [X_p \, g^1_F(q,t)]^2 + 2X_p(1-X_p)\, g^1_F(q,t) + 1 \qquad (14)$$

where $X_p = \langle I_F \rangle_T / \langle I_E \rangle$ is the ratio of the thermal dynamic scattering intensity to the total scattering intensity and $g^1_F(q,t)$ is the field correlation function of the thermally fluctuating component, which is described by an exponential decay similar to Equation (12). The heterodyne diffusion coefficient, D_{HT}, can be accordingly obtained from the specific correlation time according to Equation (13), which in turn associates to the correlation length, ξ, through the Stokes–Einstein equation.

$$\xi = \frac{k_B T}{6\pi\eta D_{HD}} \qquad (15)$$

Here, ξ is a measure of the scale of the concentration fluctuations of the dynamic component, which can be correlated to the network mesh size. The field correlation functions of two representative positions, corresponding to speckles with a high and a low scattering intensity, for the plain chemical network at 60°, are shown in Figure 3b. The solid curves show the fits obtained

via approximating $g^1_F(q,t)$ by a single exponential function as in Equation (13). The good overlay reveals that there is only one relaxation mode in the plain chemical network. However, as the representative data of the DN-Zn sample in the inset plot of Figure 3b shows, a single exponential function does not provide a good fit for some samples, specifically at longer times. In such cases, a second long relaxation mode exists, and therefore, a bi-exponential function is required.

$$g^1_F(q,t) = a\exp(-t/\tau_1) + (1-a)\exp(-t/\tau_2) \qquad (16)$$

The DLS data are analyzed by inserting Equation (12) or (16) into Equation (14), for each sample, at all angles and every 100 positions, and the ensemble-average correlation time, τ, along with average ratio of the thermal to the overall scattering intensities, X_p, are derived and plotted against the squared magnitude of the scattering vector, q^2, as shown in **Figure 5**. The smaller standard error bars, compared to Figure 4, suggest that DLS results are statistically more reliable.

The field correlation functions of the DN-Mn and DN-Zn samples show two distinct relaxation modes in the observable time domain, while the other dually crosslinked networks demonstrate a single relaxation process. The fast relaxation process of the formers coincides with the single relaxation process of the latter. This process is correlated to the so called "collective diffusion" in gels, which originates from the network strand fluctuations.[15,17] The specific time constant of this relaxation process shows a q^2 dependence, from which the heterodyne
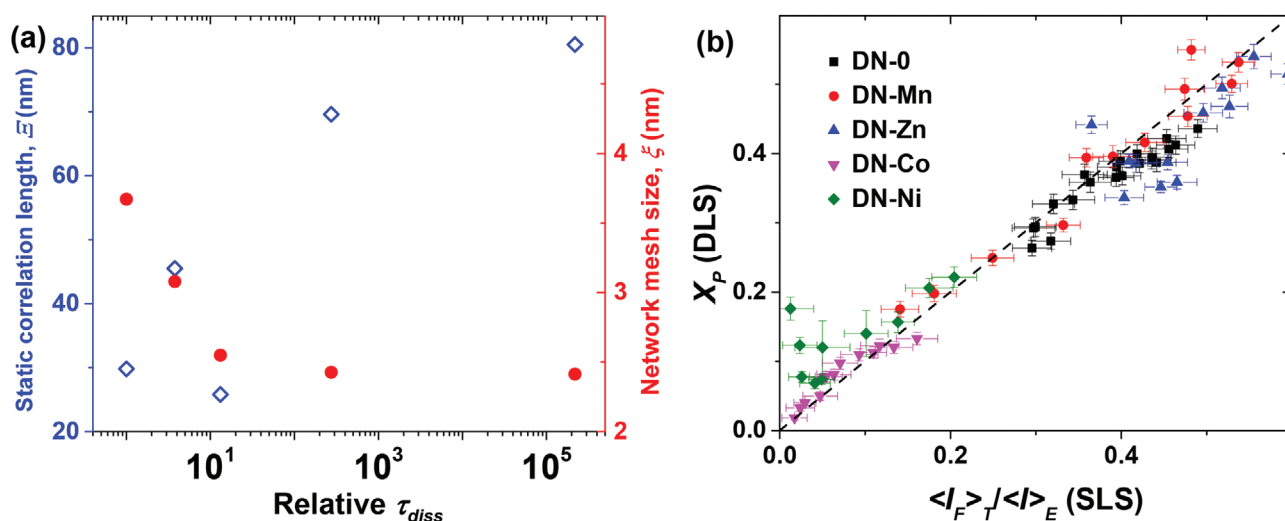
Figure 6. a) Static and dynamic correlation lengths, which can be associated with the static concentration fluctuations and network strand length, respectively, as a function of relative dissociation time of the metallo-supramolecular bonds that follows the order of Mn < Zn < Co < Ni and b) comparison of the ratio of the thermal to the overall scattering intensities obtained from independent DLS and SLS analyses. Bars represent the standard errors.

diffusion coefficient, D_{HT}, is calculated by a simple regression, as demonstrated in Figure 5. Within the experimental error limits, the regression lines pass the origin. This qualitatively suggests that the utilized single or bi-exponential functions are sufficient to capture all the physically important relaxation modes. The slow modes of the DN-Mn and DN-Zn samples show q^0 dependence, as shown in Figures 5b and 5c, respectively. Such a non-diffusive relaxation process can be attributed to either the dissociation of metallo-supramolecular bonds or fluctuations of the static inhomogeneities.[17,18] This mode is faster for DN-Mn compared to DN-Zn and is not seen in DN-Co and DN-Ni samples. Our former rheological studies suggest a similar trend in the dissociation time of the metallo-supramolecular bonds.[30] The slow relaxation process is consequently associated with the dissociation of the bis-complexes, and it is absent for the stronger Co^{2+} and Ni^{2+} ions, since their corresponding dissociation time is beyond the measured time limit (30 s).[30] The X_P values are relatively lower for the DN-Co and DN-Ni networks, as shown by the right-hand ordinate in Figure 5. This qualitatively confirms that these samples contain larger contribution of the static concentration fluctuations.

The network mesh size can be calculated from the obtained D_{HT} values using Equation (15). The outcomes, along with the static correlation lengths obtained from the SLS analysis (Figure 4), are compared for different networks in **Figure 6**a. The networks are sorted in the horizontal direction according to the relative dissociation time of their metallo-supramolecular bonds. The relative dissociation times were already obtained by studying the diffusivities of a sticky and a non-sticky linear PEG tracers within the networks.[30] The obtained results confirmed the following order for the kinetic stability of the formed metal ion–bis(terpyridine) complexes, Mn < Zn < Co < Ni. The average network mesh size decreases with increasing association tendency of the utilized ion from 3.8 nm for the plain chemical network to 3 nm for the DN-Mn and to 2.6 nm for the DN-Zn sample, but remains constant upon going to DN-Co and DN-Ni, as shown by the filled symbols in Figure 5a. This

qualitatively implies that the Mn^{2+} ion forms less than two associations per strand, while the other ions bond quantitatively. Our former analysis of the rheological behavior using the sticky Rouse model also provided very comparable results.[30]

The static correlation lengths are about ten times larger than the network mesh sizes. The obtained values are relatively larger for the DN-Co and DN-Ni networks compared to the other samples, but unlike the network strand lengths, they do not follow a smooth trend. This is consistent with our former hypothesis that such strongly associating ions form collective assemblies.[30] It was speculated that the complexed metal ions and the counter ions in solution have strong binding Coulomb interactions, which mediates the formation of nanoscopic salt clusters even in the solution. This hypothesis might be further confirmed using direct microscopy imaging techniques.

Finally, we compare the results obtained from the independent SLS and DLS analyses for the ratios of the thermal to the overall scattering intensities, as shown in Figure 5b. The obtained results confirm each other and the accuracy of both analysis methods. Moreover, they indicated once again that the DN-Co and DN-Ni samples exhibit lower contributions of the dynamic component while the other samples have similar compositions, which again supports the larger static concentration fluctuations in former samples that could be correlated to the formation of collective assemblies. In the following section, we provide a more quantitative insight into network inhomogeneities and possible clustering by analyzing the double-quantum NMR responses of the samples.

3.2. ¹H DQ NMR

To further elucidate the contributions of the possible collective assemblies, local inhomogeneities, and different connectivities of this system, we apply static time-domain ¹H DQ NMR. It provides quantitative information on the strength, amount, and possibly distribution of proton–proton dipolar couplings, which

ADVANCED
SCIENCE NEWS
www.advancedsciencenews.com

Macromolecular
Chemistry and Physics
www.mcp-journal.de

encode the local amplitude of motion of the backbone segments on the scale of individual network strands.[33,34] It thus provides a chain-level measure of the network mesh size and possible inhomogeneities. The proton–proton dipolar coupling is proportional to the second Legendre polynomial $P_2[\cos \theta]$, where θ is the angle between the internuclear proton–proton connection vector and the static magnetic field. Assuming a multispin network and fast oriental averaging by the segmental motions (far above T_g, being fulfilled in a gel), we expect to measure a single effective RDC constant, D_{res}, that is representing all monomers of a given chain (D_{res} is in units of rad s^{-1}, thus $D_{res}/2\pi$ is in Hz).[33] Without any segmental reorientations on that scale, the observed coupling would attain a maximum value, representing an effectively static Kuhn segment. Due to motions of the individual monomers within a Kuhn segment, which effectively reorient uniaxially around the backbone axis, this dipolar coupling representing the static Kuhn segment is also averaged to an effective value D_{eff}. If the chain is now fluctuating and constrained by crosslinks or entanglements, D_{res} is much lower but finite and can be measured using the DQ experiment.

Neglecting the influence of entanglements and assuming Gaussian statistics, a simple expression for the dependency of the RDC on the number of network chain segments N is found.[43]

$$D_{res} = D_{eff}\ S_b = D_{eff}\ \frac{3}{5N}\left(\frac{R}{R_0}\right)^2 \qquad (17)$$

here, R_0 is the equilibrium end-to-end distance in semidilute solution, and R is the actual end-to-end distance including possible stretching of the chains due to the swelling of the network. As the networks in both cases (scattering and NMR) were measured in "as-prepared" conditions, this factor is equal to 1. If this were not the case, D_{res} would be dependent on the volume degree of swelling ($Q = V/V_0$), and further differences arise from excluded volume effects in a good rather than a theta solvent.[43] For networks crosslinked in bulk, D_{res} initially decreases with increasing Q (due to excluded-volume effects as well as relief of entanglements), but eventually increases with increasing Q at higher swelling degrees due to the (ideally) affine stretching of the chains.[44] To avoid such ambiguities and to compare the RDC of different samples with light scattering results, the same Q was realized for all samples.

An important factor that strongly distorts the simple inverse relationship of the observed RDC and the network mesh size was recently discussed[45–47] and summarized:[45] The existence of loop defects, as illustrated in **Figure 7**, increases the effective mesh size (leading to a reduction of D_{res}) by, for example, a factor of 2 in the case of connecting two four-arm-stars with parallel linear linkers, constituting a secondary loop. The center of Figure 7 shows a primary loop of order 4, and the top shows a primary loop, which is formed by the metallo-supramolecular bonds, that does not bear any load ($D_{res} = 0$). In particular these are commonly expected in a system involving linear precursors.[48] Therefore, the reader needs to be aware that simple back-of-the-envelope calculations using a model system (e.g., tetra-PEG), measured RDC values, and the obtained mesh sizes by light scattering cannot be related directly without fur-
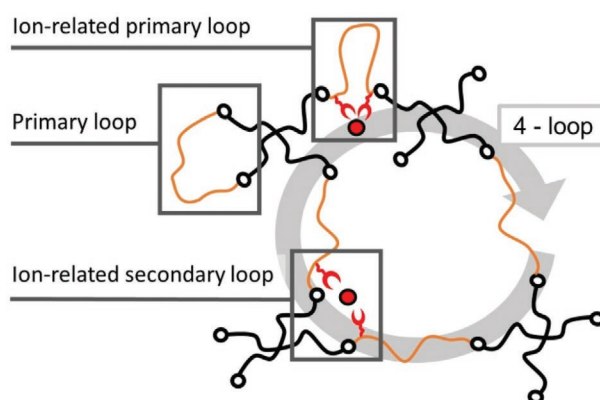

Figure 7. Typical loop structures in a metallo-supramolecular dual-network. Without the addition of metal ions (DN-0), the network would consist only of the loop-containing mesh formed by the four-arm star and the linear chain (see Figure 1), with additional non-elastic defects that do not involve metal ions such the primary loop defect shown on the upper left and dangling chains (not shown). The addition of metal ions may introduce further loop defects.

ther assumptions, and one needs to take possible misconnectivities into account.

Starting with the chemical network without addition of metal ions, we observe that even in this simple case, a single A-l function or even a Gaussian-distribution of D_{res} is not sufficient to fit the data. Thus, a summation of two distinct A-l functions is needed, as the option with the least amount of parameters, which fits the data sufficiently. This is expected, as the four-arm-star systems usually show a distinct set of connectivities instead of a broad size distribution of the same connectivity.[37] In the present case, with a star precursor and a linear precursor, we expect mostly two types of connectivities: The primary network mesh (with a finite RDC) is the simple, desired connection of a single linear and two different stars, and the second connection that occurs with a high probability is the primary loop (see Figure 7), where the linear PEG binds with two arms of the same star PEG. We expect such a loop to fluctuate isotropically, resulting in $D_{res} = 0$. Thus, it will constitute a significant part of the long tail of about 45% (see **Figure 8**b) that was quantified using the tail subtraction procedure. The second important contribution to this tail arises from dangling chain ends.

A fit to the nDQ data shows that a single A-l function is not sufficient to fit the data, and a distribution according to Equation (5) is needed, resulting in an average $D_{res}/2\pi$ of 2.1 Hz and a lognormal distribution width of 0.5 (see Figure 8a). The reason for this distribution is probably the significant defect fraction, which, as already mentioned above, has an influence on the effective mesh size. Its fraction of 45% already indicates that for most of the star precursors we expect more than just one loop per chain. As those defects are stochastically distributed over each network mesh, we expect a corresponding distribution in size and thus in measured RDCs.

As already mentioned, a precise back-of-the-envelope calculation for comparison of the obtained RDC with the tetra-PEG system[37] is hardly possible, but it gives a hint about the defects present in the network. The obtained $D_{res}/2\pi$ for the chemical
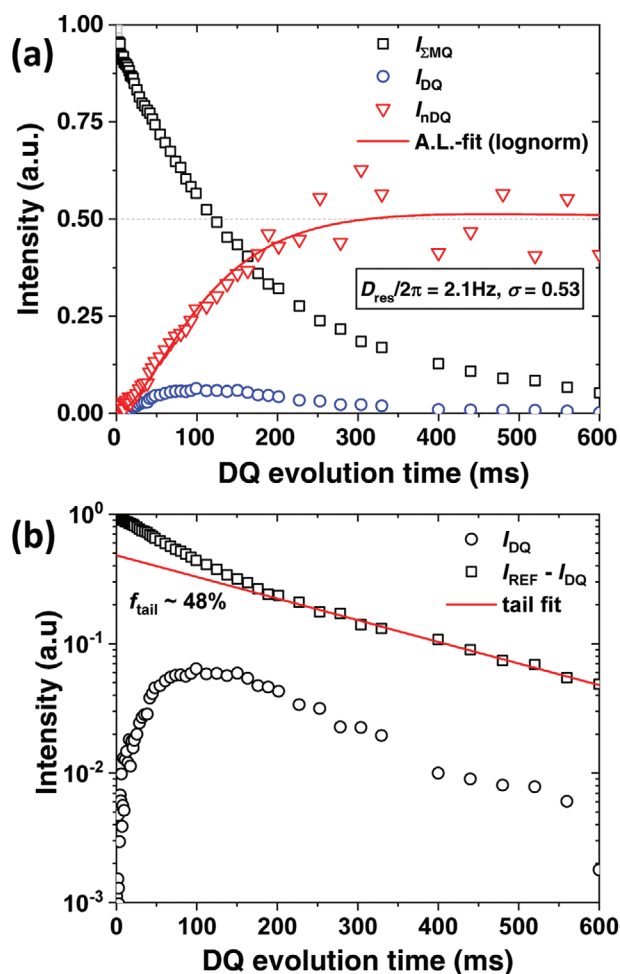
Figure 8. a) Overview of the measured signals ($I_{\Sigma MQ}$ and I_{DQ}) for the chemical network without ions, DN-0, and the resulting normalized DQ-buildup curve after tail subtraction, which was calculated using Equation (3). b) Semi-logarithmic plot of $I_{REF} - I_{DQ}$ for a more pronounced visualization of the tail.[49] I_{DQ} is plotted just as an orientation.

network is about 2 Hz, whereas the tetra-PEG single link with a weight average molar mass of 5 kg mol^{-1} has an RDC of 70 Hz.[37] A reduction factor of about 2.2 is already found by size comparison. The tetra-PEG mesh consists of two arms with 2.5 kg mol^{-1} each, whereas our system has an additional 6 kg mol^{-1} linear PEG in between. Using the recent results of Lang that were mentioned above,[45] we find another factor of 2, assuming each four-arm star has a loop, turning the star into a linear extender. This may even increase if we also consider dangling chains and higher order loops. This yields a total factor of about 4.4, which means that there is still a factor of about 7 missing. Summing up, we cannot provide a precise calculation, but even the fact that those two values are more different than a factor of 2 (as provided by the size comparison) indicates the central importance of topological network defects.

As metal ions are introduced into the system, the network will change due to the physical crosslinking of two adjacent linear precursors through their terpyridine functionalities (see Figure 7). This process is supposed to be dependent on the ionic strength and binding efficiency. One can immediately see the
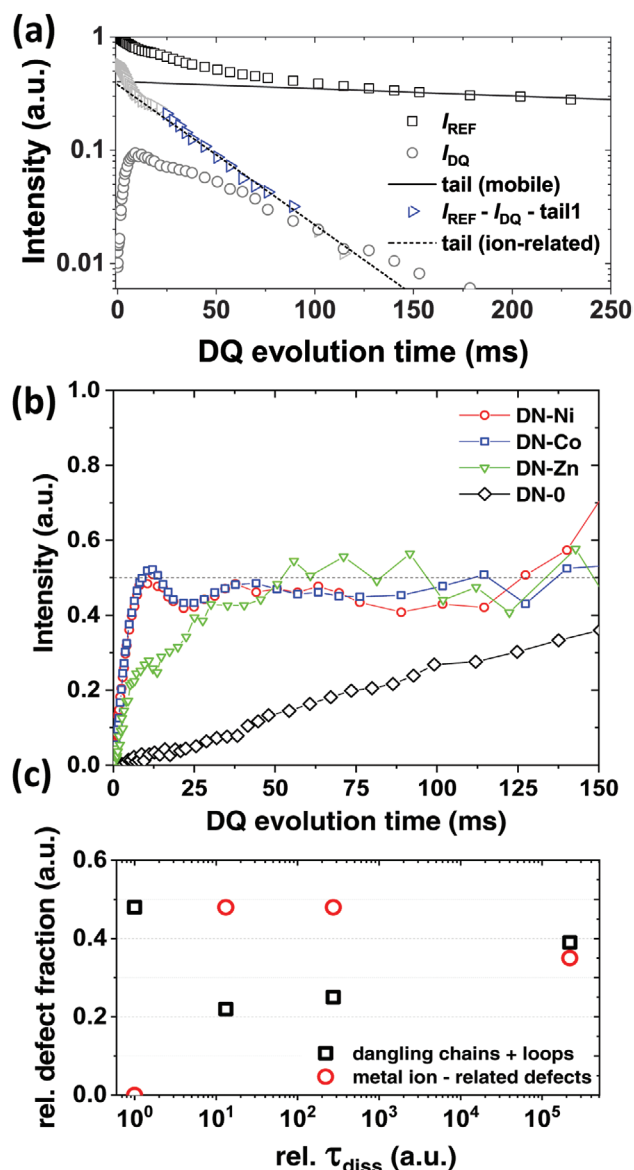

Figure 9. a) Example double-tail subtraction using I_{ref}-I_{DQ}-tail 1.[49] b) Normalized DQ-build-up curves for metal containing dual-networks plotted together with the chemical network DN-0 as a comparison. Dual-network hydrogels have two additional components in the build-up curve acting on shorter timescales, corresponding to higher RDC constants. c) Estimated relative defect densities (after water signal subtraction and renormalization) using the double-tail subtraction procedure and additionally the T_1 relaxation data (see Appendix A) obtained from the saturation recovery experiment.

effects of this additional crosslinking in the normalized build-up curve (see **Figure 9**b), as now there is a significant build-up component on a short timescale, corresponding to a relatively higher RDC (more immobilized chains). Additionally, a new defect is introduced, which is noticeable by the incapability of normalizing I_{nDQ} to 0.5 by using only the single long-time tail (not shown). This new defect has a shorter T_2 (≈ 50 ms) (see Figure 9a,c) and can be clearly associated with misconnectivities that are realized after the introduction of the metal ions. It is most likely associated with a metal ion linking the two TPy
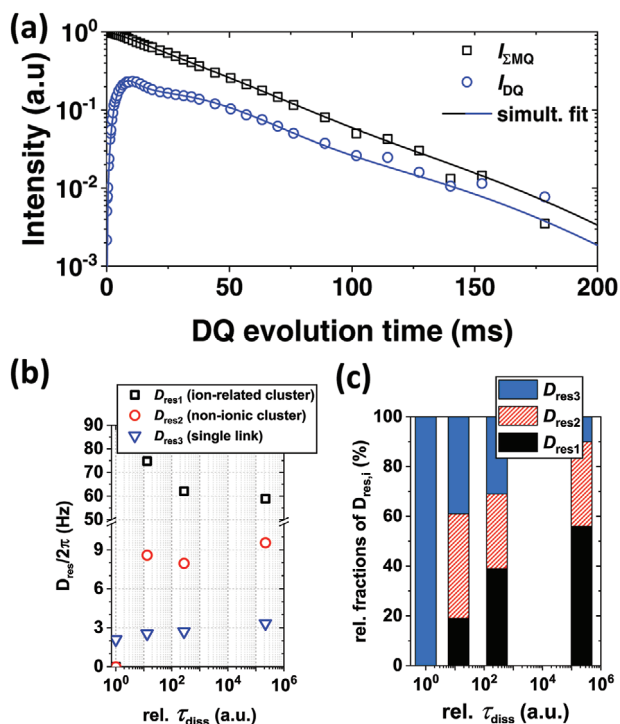
ADVANCED
SCIENCE NEWS
www.advancedsciencenews.com

Macromolecular
Chemistry and Physics
www.mcp-journal.de

Figure 10. a) Example data (DN-Ni) with simultaneous fitting result. b) Size of the RDCs depending on τ_{diss}. c) Overview of the fractions per RDC as obtained from the fit. The amount of non-reinforced single-link structures decreases with increasing rel. bond dissociation time τ_{diss}, whereas the fraction of the RDC supposedly corresponding to the ion-related network clusters increases with increasing τ_{diss}.

functionalities of a given linear PEG chain resulting in a primary loop (see Figure 7). Its reduced mobility may explain the shorter T_2 relaxation.

Note that the sample DN-Mn could not be studied by DQ NMR due to very fast T_2 relaxation arising from nuclear-electron hyperfine coupling to the paramagnetic ion. Somewhat unexpectedly, such an effect was absent in the also paramagnetic DN-Co and DN-Ni, probably because of comparably fast electron T_1 relaxation and the resulting averaging of the hyperfine coupling. As the standard usage of A-l functions for the nDQ data does not work anymore, we use the fitting procedure presented above for fitting I_{DQ} and $I_{\Sigma MQ}$ simultaneously assuming a distinct set of RDC values with different relaxation times. The used fitting procedure does not assume a distribution for the individual RDCs, due to possible interdependencies between the parameters and moreover since the data is fitted well enough without these additional parameters. An example data work-up is shown in **Figure 10**a, and fit results are shown in Figure 10b,c. The three obtained RDC values corresponding to the three buildup components that are observed in the nDQ data and—although less pronounced—visible in the I_{DQ}-data are on the order of roughly 70, 9, and 3 Hz, respectively (see Figure 10b,c).

The assignment of those different components found in the normalized buildup curves to the actual types of network connectivity and defects is not trivial. Schwenke and coworkers had used a Monte Carlo simulation based on the bond-fluctuations model to compare the fraction of different network connectivity

defects with the experimental finding, in an ideal chemically crosslinked tetra-PEG network.[50,51] This is not done in this work, but as the smallest value (3 Hz) is already known from the chemical network with only little deviation, we assume that arises from the same structure, which is the single link of linear PEG and tetra-PEG. The increase of this RDC eventually gives a hint about the decreased network mesh size.

The assignment of the remaining two RDCs can be discussed on the basis of the results obtained from the light scattering experiments above. According to the significant fraction of defects related to the introduction of metal-ions, we expect that not every network mesh is reinforced by the metal ions despite the stoichiometric ratio between TPy functionalities and metal ions. Thus, we assume that we observe two different RDCs corresponding to the chemical network without ions and the reinforced dual-network mesh, respectively. The former is already assigned (see above) and the latter will have an increased RDC, which we assume to correspond to the measured D_{res} of about 9 Hz. The remaining coupling of about 60–70 Hz is larger by a factor of 35, which does not seem realistic for the reinforced network.

Still, this apparently highly crosslinked component is present in significant amounts, and the amount displays a direct correlation with increasing relative bond dissociation time. Here, we do not claim a direct connection to this slow process, but rather take the increased bond dissociation time as a measure of reactivity. Faster ion-induced network formation, which competes with the formation of chemical connections, will have a significant impact on the structure that is then fixed chemically. Thus, ion-related inhomogeneities are effectively imprinted in the chemical network. A similar argument probably holds for the additionally observed fraction of ion-induced primary loops (see Figure 7). Also such structures are quickly formed from a single ion and a single linear chain, and the spatial correlation of the chain ends is then fixed chemically. Therefore, we can directly prove the hypothesis mentioned above in the light scattering part that essentially claims the existence of collective assemblies emerging from the nano-phase separation of the strong ions in the system.

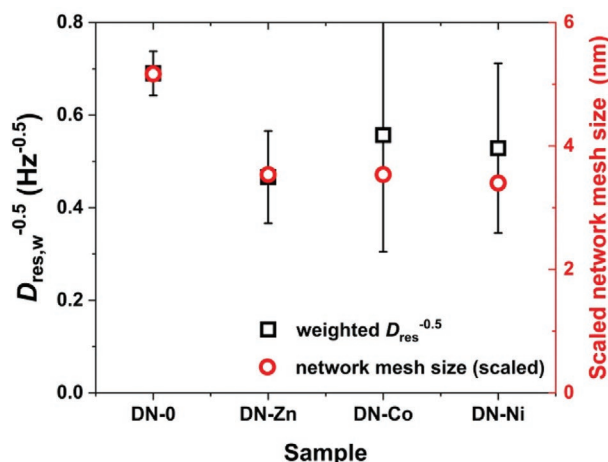Finally, **Figure 11** provides a direct comparison of the mesh size information available from NMR and LS. For this

Figure 11. Direct comparison of average mesh sizes from NMR (left; weighted average of D_{res1} and D_{res2}, plotted as inverse root) and from LS (right) for all samples.

comparison, we need to consider that the LS-based correlation length is $\xi \approx lN^\nu$ with $\nu = 0.6$ in good solvent and N the effective number of segments. For NMR, in turn, Equation (17) is somewhat modified in good solvent, where $D_{res} \approx N^{-2\nu}$.[43] Therefore, we compare ξ with $D_{eff}^{-0.5}$, where D_{eff} is the weighted average of D_{res1} and D_{res2} in the dual-networks. These two components are expected to dominate the larger-scale structure probed by LS.

We notice a good agreement of the results (rescaled to match for DN-0) across the sample series, despite the relative large uncertainty for two of the ion samples. One also needs to keep in mind that the comparison is hardly expected to be quantitative because D_{res} (in much the same way as the elasticity modulus) is further modulated by the elastic effectiveness of the network strands subject to their immediate topological environment. It depends sensitively on the order of possible loop structures it is part of, as opposed to the infinite branched tree assumed in phantom network theory. This has only recently been recognized and discussed,[45–47] and subtle topological differences among the different ion samples may well exist.

4. Conclusions

The network structure and the dynamics of reversible bonds have well-known effects on the macroscopic properties of single networks based on purely chemical or purely physical crosslinks, respectively. However, their individual effects and interplay are complicated when chemical and physical bonds are combined in a dual network. This is pronounced both in the dynamics and the structure of the resulting material. For instance, our former studies on the dynamic mechanical properties of dual-networks show that the strength of the reversible bonds can be manipulated by the network structure and vice versa. To further deconvolute this complexity, here we studied the structure and inhomogeneities of these materials using light scattering and proton double-quantum NMR. This is realized by using a linear PEG precursor whose terminal functional groups form an instantaneous click reaction with the terminal groups of another tetra-arm PEG precursor. The linear precursor also carries a terpyridine ligand at each end, which forms metallo-supramolecular bonds with adjustable strength by the addition of different metal ions. DLS suggests that the network mesh size approaches a steady value by increasing the association tendency of the metal ion. This is quantitatively supported by increasing RDC constants associated with the single network links in DQ NMR analysis. SLS shows higher static concentration fluctuations for gels connected through stronger ions. This is accompanied by a fast solid-like relaxation in DQ NMR, whose contribution also increases by the association affinity of the metallo-supramolecular bonds. This solid body can be correlated to the formation of nanosized clusters by phase-separation of the metal ions. Moreover, DQ NMR suggests that the presence of the physical bonds cause further local inhomogeneities, specifically loops, in the structure of the forming chemical network, as comprehended by a larger fraction of mobile segments for networks consisting of stronger ions. These results unveil the interplay of the physical and the chemical bonds in the structure and macroscopic properties of dual networks, which can help in designing materials based on this concept.

Conflict of Interest

The authors declare no conflict of interest.

[1] J. P. Gong, *Soft Matter* **2010**, *6*, 2583.

[2] J. P. Gong, Y. Katsuyama, T. Kurokawa, Y. Osada, *Adv. Mater.* **2003**, *15*, 1155.

[3] J. A. Neal, D. Mozhdehi, Z. Guan, *J. Am. Chem. Soc.* **2015**, *137*, 4846.

[4] J.-Y. Sun, X. Zhao, W. R. Illeperuma, O. Chaudhuri, K. H. Oh, D. J. Mooney, J. J. Vlassak, Z. Suo, *Nature* **2012**, *489*, 133.

[5] O. Chaudhuri, L. Gu, M. Darnell, D. Klumpers, S. A. Bencherif, J. C. Weaver, N. Huebsch, D. J. Mooney, *Nat. Commun.* **2015**, *6*, 6365.

[6] M. Guo, L. M. Pitet, H. M. Wyss, M. Vos, P. Y. Dankers, E. Meijer, *J. Am. Chem. Soc.* **2014**, *136*, 6969.

[7] X. Hu, M. Vatankhah-Varnoosfaderani, J. Zhou, Q. Li, S. S. Sheiko, *Adv. Mater.* **2015**, *27*, 6899.

[8] G. Li, H. Zhang, D. Fortin, H. Xia, Y. Zhao, *Langmuir* **2015**, *31*, 11709.

[9] P. Lin, S. Ma, X. Wang, F. Zhou, *Adv. Mater.* **2015**, *27*, 2054.

[10] J. Liu, C. S. Y. Tan, Z. Yu, Y. Lan, C. Abell, O. A. Scherman, *Adv. Mater.* **2017**, *29*, 1604951.

[11] C. H. Yang, M. X. Wang, H. Haider, J. H. Yang, J.-Y. Sun, Y. M. Chen, J. Zhou, Z. Suo, *ACS Appl. Mater. Interfaces* **2013**, *5*, 10418.

[12] P. Malo de Molina, S. Lad, M. E. Helgeson, *Macromolecules* **2015**, *48*, 5402.

[13] S. Seiffert, *Polym. Chem.* **2017**, *8*, 4472.

[14] S. Seiffert, *Prog. Polym. Sci.* **2017**, *66*, 1.

[15] M. Shibayama, *Bull. Chem. Soc. Jpn.* **2006**, *79*, 1799.

[16] T. Sakai, T. Matsunaga, Y. Yamamoto, C. Ito, R. Yoshida, S. Suzuki, N. Sasaki, M. Shibayama, U.-i. Chung, *Macromolecules* **2008**, *41*, 5379.

[17] T. Rossow, A. Habicht, S. Seiffert, *Macromolecules* **2014**, *47*, 6473.

[18] T. Rossow, S. Seiffert, *Polym. Chem.* **2014**, *5*, 3018.

[19] S. Tang, A. Habicht, S. Li, S. Seiffert, B. D. Olsen, *Macromolecules* **2016**, *49*, 5599.

[20] W. C. Yount, D. M. Loveless, S. L. Craig, *J. Am. Chem. Soc.* **2005**, *127*, 14488.

[21] E. A. Appel, F. Biedermann, D. Hoogland, J. Del Barrio, M. D. Driscoll, S. Hay, D. J. Wales, O. A. Scherman, *J. Am. Chem. Soc.* **2017**, *139*, 12985.

[22] E. A. Appel, R. A. Forster, A. Koutsioubas, C. Toprakcioglu, O. A. Scherman, *Angew. Chem.* **2014**, *126*, 10202.

[23] Y.-H. Na, T. Kurokawa, Y. Katsuyama, H. Tsukeshiba, J. P. Gong, Y. Osada, S. Okabe, T. Karino, M. Shibayama, *Macromolecules* **2004**, *37*, 5370.

[24] T. Nakajima, H. Furukawa, Y. Tanaka, T. Kurokawa, J. P. Gong, *J. Polym. Sci., Part B: Polym. Phys.* **2011**, *49*, 1246.

[25] T. Nakajima, Y. Fukuda, T. Kurokawa, T. Sakai, U.-i. Chung, J. P. Gong, *ACS Macro Lett.* **2013**, *2*, 518.

[26] H. Kamata, Y. Akagi, Y. Kayasuga-Kariya, U.-i. Chung, T. Sakai, *Science* **2014**, *343*, 873.

[27] S. Kondo, T. Hiroi, Y. S. Han, T. H. Kim, M. Shibayama, U. i. Chung, T. Sakai, *Adv. Mater.* **2015**, *27*, 7407.

[28] T. Hiroi, S. Kondo, T. Sakai, E. P. Gilbert, Y.-S. Han, T.-H. Kim, M. Shibayama, *Macromolecules* **2016**, *49*, 4940.

[29] S. Czarnecki, T. Rossow, S. Seiffert, *Polymers* **2016**, *8*, 82.

[30] M. Ahmadi, S. Seiffert, *J. Polym. Sci., Part A: Polym. Chem.* **2019**, unpublished.

[31] M. Ahmadi, A. Jangizehi, E. Van Ruymbeke, S. Seiffert, *Macromolecules* **2019**, *52*, 5255.

[32] W. Schmolke, M. Ahmadi, S. Seiffert, *Phys. Chem. Chem. Phys.* **2019**, *21*, 19623.

[33] K. Saalwächter, *Prog. Nucl. Magn. Reson. Spectrosc.* **2007**, *51*, 1.

[34] K. Saalwächter, *ChemPhysChem* **2013**, *14*, 3000.

[35] W. Chassé, J. L. Valentín, G. D. Genesky, C. Cohen, K. Saalwächter, *J. Chem. Phys.* **2011**, *134*, 044907.

[36] L. Jakisch, M. Garaleh, M. Schäfer, A. Mordvinkin, K. Saalwächter, F. Böhme, *Macromol. Chem. Phys.* **2018**, *219*, 1700327.

[37] F. Lange, K. Schwenke, M. Kurakazu, Y. Akagi, U.-i. Chung, M. Lang, J.-U. Sommer, T. Sakai, K. Saalwächter, *Macromolecules* **2011**, *44*, 9666.

[38] D. Mozhdehi, J. A. Neal, S. C. Grindy, Y. Cordeau, S. Ayala, N. Holten-Andersen, Z. Guan, *Macromolecules* **2016**, *49*, 6310.

[39] M. H. Jandaghian, S. Ahmadjo, M. M. Mortazavi, M. Ahmadi, *Appl. Organomet. Chem.* **2019**, unpublished.

[40] M. Asai, T. Katashima, U.-i. Chung, T. Sakai, M. Shibayama, *Macromolecules* **2013**, *46*, 9772.

[41] T. Matsunaga, T. Sakai, Y. Akagi, U.-i. Chung, M. Shibayama, *Macromolecules* **2009**, *42*, 6245.

[42] J. G. Joosten, J. L. McCarthy, P. N. Pusey, *Macromolecules* **1991**, *24*, 6690.

[43] J.-U. Sommer, W. Chassé, J. L. Valentín, K. Saalwächter, *Phys. Rev. E* **2008**, *78*, 051803.

[44] W. Chassé, S. Schlögl, G. Riess, K. Saalwächter, *Soft Matter* **2013**, *9*, 6943.

[45] M. Lang, *Macromolecules* **2019**, *52*, 6266.

[46] T.-S. Lin, R. Wang, J. A. Johnson, B. D. Olsen, *Macromolecules* **2019**, *52*, 1685.

[47] S. Panyukov, *Macromolecules* **2019**, *52*, 4145.

[48] W. Chassé, M. Lang, J.-U. Sommer, K. Saalwachter, *Macromolecules* **2012**, *45*, 899.

[49] K. Saalwächter, M. Klüppel, H. Luo, H. Schneider, *Appl. Magn. Reson.* **2004**, *27*, 401.

[50] I. Carmesin, K. Kremer, *Macromolecules* **1988**, *21*, 2819.

[51] K. Schwenke, M. Lang, J.-U. Sommer, *Macromolecules* **2011**, *44*, 9464.